**Geomechanics and Engineering,** *Vol. 46, No. 1 (2026) 27-51*
https://doi.org/10.12989/gae.2026.46.1.027

# Experimental study on the morphological characteristics of artificially split rock joints and their controlling factors

Seungbeom Choi*, Taehyun Kim, Seong Jun Ha, Saeha Kwon, Jin-Seop Kim

*Korea Atomic Energy Research Institute, 111, Daedeok-daero 999 beon-gil, Yuseong-gu, Deajeon, 34057, Republic of Korea*

*(Received February 18, 2026, Revised April 12, 2026, Accepted May 18, 2026)*

**Abstract.** Understanding the thermal-hydraulic-mechanical behavior of rock joints is essential in many civil and rock engineering applications, but controlled testing on natural joints is often impractical. This study investigates artificial tensile joints generated by wedge-splitting in medium- to coarse-grained granite specimens and evaluates the effects of loading rate, specimen size, and loading direction on surface morphology. Block and cylindrical specimens were tested under loading rates of 0.0001~0.01 mm/s. Joint surfaces were digitized via 3D laser scanning; directional profiles at 15° increments were used to compute three roughness parameters including CLA (Center Line Average), Z2 (root mean square of the first derivative of a profile), and fractal dimension (D). Spatial correlation was quantified using the experimental variogram with spherical fits to obtain range and sill. No discernible rate dependency was detected in either roughness or variogram parameters within the tested range. Size effects were parameter-specific: CLA increased with specimen size, whereas Z2 and D were relatively higher in the smallest specimens. Roughness showed a clear directional effect, being greater perpendicular to the loading axis than parallel. Variogram parameters increased with size (both range and sill), while directional differences in spatial correlation were weak and generally not statistically significant. Consistent with the amplitude-correlation relationship, the sill related to CLA, and a normalized initial slope ($\sqrt{sill/range}$) qualitatively related to Z2 and D. Overall, specimen size and loading direction govern the scale of roughness that is emphasized, providing practical guidance for the design and interpretation of experiments using artificial joint specimens.

**Keywords:** artificial rock joint; directionality; loading rate; morphological characteristics; specimen size; splitting test

## 1. Introduction

Rock joints exert a significant influence on the thermal-hydraulic-mechanical (THM) behavior of rock masses, which is critical in various engineering applications. Examples include the design and construction of underground structures, such as deep underground tunnels, storage facilities, and repositories for the disposal of high-level radioactive waste, as well as $CO_2$ sequestration, geothermal energy extraction, and groundwater utilization. Mechanically, rock joints constitute weak planes within rock masses. Hydraulically, they act as preferential flow pathways for fluid, significantly affecting the flow behavior within rock masses. Therefore, understanding the effects of rock joints under coupled THM processes through theoretical, experimental, and numerical

*Corresponding author, Ph.D., E-mail: sbchoi26@kaeri.re.kr


http://www.techno-press.org/gae/5
ISSN: 2005-307X (Print), 2092-6219 (Online)

approaches has been a long-standing research objective in many fields of geomechanics [1-6]. Numerous studies have been conducted, employing joint specimens tailored to specific experimental objectives [7-10]. Characterizing joint properties, such as surface morphology, strength, deformation, and hydraulic behavior, provides the fundamental data required for a wide range of engineering projects. Based on such results, theoretical and numerical analyses are applied to tunneling, underground storage, slope and foundation design, site characterization, and the modelling of the coupled THM behavior of rock masses.

To represent in situ conditions and the geological characteristics of a specific study site, it is ideal to use natural joints sampled from the local rock formation. However, when natural joints are limited in their geometry, conditions, or quantity, laboratory-generated joint specimens are frequently used as a practical alternative. Despite ongoing debates about the feasibility of artificial joints as substitutes for natural ones [11, 12], they are still widely adopted. Artificial joints are typically produced by splitting tests, most often the Brazilian tension test for rock cores [11, 13, 14], while a wedge-shaped loading frame is frequently used for block specimens because it provides reliable contact and boundary conditions [10, 15-17]. Notably, specimen geometry and loading configu-ration govern crack initiation and propagation and thus shape the resulting surface morphology.

Rock joint morphology is characterized by several geometric properties, such as roughness, aperture, matedness, spatial correlation, and many others, which, in turn, affect coupled THM behavior. To achieve reproducibility in experiments focusing on the geometric properties of rock joints, replicas made from cement mortar or plaster have been widely adopted [18-20]. These materials allow the duplication of joint surfaces, thereby facilitating controlled experimental conditions. Recently, 3D printing technology has also been increasingly adopted to replicate the geometric features of rock joints [21-23]. Despite the advantages of these approaches, they have inherent limitations in simulating the brittle behavior of rock, especially that of crystalline rocks, and in accurately reproducing micro-scale joint asperities. In particular, mismatches in elastic-plastic properties and finite layer resolution can bias measurements of shear strength and hydraulic properties. Therefore, artificial joint specimens produced by splitting still retain advantages, as they better simulate brittle failure and preserve micro-scale asperities, yielding a more accurate representation of the mechanical and hydraulic behavior of rock joints.

Several studies have analyzed the geometric characteristics of artificial joints generated by splitting tests and the experimental factors that influence them. For example, Babadagli and Develi [24] reported that the fractal dimension decreases with increasing loading rate and grain size. Cui et al. [25] found that joint roughness increases with increasing loading rate, whereas Shams et al. [26] reported that roughness increases with decreasing loading rate. Khosravi et al. [27] investigated the effects of loading direction and specimen shape (i.e., the height to diameter ratio of a rock disc) on joint roughness, and Vogler et al. [11] reported that smaller specimens tend to exhibit lower roughness when failure is governed by specimen dimensions. In addition, Zhang et al. [28] reported that roughness increases with the degree of saturation. Although the aforementioned studies have reported various experimental results, the number of studies investigating these factors remains limited relative to the widespread use of artificial joint specimens. Moreover, previous studies have shown some inconsistencies, specifically regarding the effect of loading rate and/or specimen size on the morphological features of split rock joints. These discrepancies likely stem from differences in lithology, specimen size and shape, surface measurement resolution, and the roughness parameters applied.

Therefore, this study aims to analyze the effects of experimental factors in splitting tests on the geometric characteristics of artificially generated rock joints. The tested material was a medium- to coarse grained crystalline granite. It was selected as the target rock type because it is one of the most widely distributed rock types in Korea and is also regarded as a relevant candidate host rock for a future geological disposal system for high-level radioactive waste. Accordingly, the present work provides experimental reference data for a rock type of particular geological and engineering importance, while future studies are required to evaluate the broader applicability of the findings to other lithologies.

To generate the artificial joints, a pair of diametrically opposed notches was carefully designed on the specimen periphery at the loading contacts. Loading rates ranging from 0.0001 to 0.01 mm/s were applied to evaluate their influence on joint surface geometry, and both block and cylindrical specimens were tested to examine the effect of specimen size and/or geometry. The split surfaces were digitized using a 3D laser scanner to obtain high-resolution topography for geometric analyses. The morphological properties considered in this study were joint roughness and the spatial correlation of surface elevation, including their directional variability. The novelty of this study lies in providing an integrated characterization of artificial tensile joints using multiple complementary descriptors of surface morphology. By combining amplitude-, slope-, and fractal-based parameters with variogram-based spatial correlation analysis, this study aims to clarify how different experimental factors govern different scales and aspects of joint morphology while also providing reference data useful for experimental design and model calibration.

The structure of the paper is as follows. After the introduction, Section 2 outlines the experimental setup, including specimen preparation by the splitting test, the acquisition of surface coordinates using a 3D scanner, and the preprocessing required to utilize the surface data. Section 3 describes the methodologies adopted for evaluating morphological characteristics, i.e., joint roughness and spatial correlation, and their directionality. Section 4 presents the experimental results and discussion, with a detailed assessment of the influence of experimental factors, including loading rate, specimen size, and directionality, on surface roughness and spatial correlation. Section 5 concludes the paper by summarizing the main outcomes and their implications for experimental design.

## 2. Experimental setup

### 2.1 Specimen preparation

The rock type used in this study was a medium- to coarse-grained granite. Intact block and cylindrical specimens were obtained from a quarry in Hwangdeung-myeon, South Korea. The granite is known to have formed during the Jurassic period of the Mesozoic era. Hwangdeung granite is predominantly medium- to coarse-grained, with its main constituent minerals including quartz, micro-quartz, alkali feldspar, plagioclase, and biotite. All the intact specimens used in this study were very fresh and exhibited no noticeable anisotropic fabrics. Fig. 1 shows the specimen geometries and dimensions, grouped into block and cylindrical types

The block specimens (denoted as BL) had nominal dimensions of 130 × 120 × 150 mm$^3$. A total of 15 block specimens were prepared, sequentially numbered from BL1 to BL15. The cylindrical specimens, with a diameter of approximately 53 mm, were prepared in two different lengths to investigate the size or shape effect. The shorter cylindrical specimens (referred to as CS) were approximately 75 mm in length, and a total of 15 cylinders were labeled sequentially from

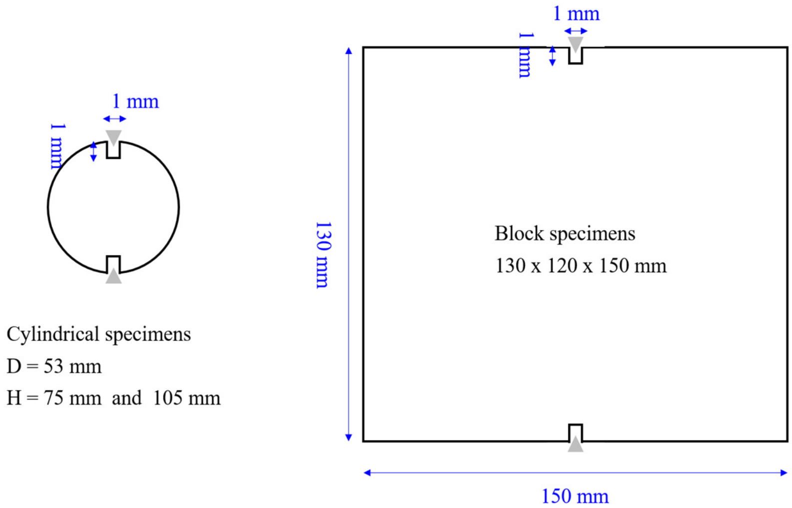


Figure 1. Specimen geometries and dimensions. Block (BL) and cylindrical specimens (CL and CS) with nominal sized indicated; opposed notch locations for wedge-splitting are shown schematically

CS1 to CS15. The longer specimens (designated as CL) were approximately 105 mm in length, with specimens numbered sequentially from CL1 to CL15. Both end surfaces of the cylindrical and all surfaces of the block specimens were grinded to satisfy the general requirements of rock mechanics tests regarding flatness, parallelism, and perpendicularity. Prior to testing, all specimens were oven-dried at 105°C for at least 24 hours to ensure dry conditions and were subsequently tested at room temperature.

To characterize the intact rock material, ten additional specimens were tested for the following fundamental properties: porosity and specific gravity, uniaxial compression (yielding the uniaxial compressive strength, Young's modulus, and Poisson's ratio) and the Brazilian tension test (yielding the Brazilian tensile strength). All tests were performed in accordance with the methods suggested by the International Society for Rock Mechanics (ISRM) [29-31]. Summary statistics are reported in Table 1. Based on the measured strength, the Hwangdeung granite can be classified as a hard rock; its low porosity (less than 1%) and high brittleness index (approximately 18) suggest pronounced brittle failure

Table 1. Fundamental physical and mechanical properties of Hwangdeung granite

| | Average | Standard deviation |
|---|---|---|
| Dry S.G. (-) | 2.64 | 0.01 |
| Porosity (%) | 0.74 | 0.07 |
| UCS (MPa) | 185.93 | 8.66 |
| E (GPa) | 65.62 | 8.26 |
| v (-) | 0.32 | 0.05 |
| BTS (MPa) | 10.51 | 1.16 |

* S.G., UCS, and BTS denote specific gravity, uniaxial compressive strength, and Brazilian tensile strength, respectively

## 2.2 Splitting test

The typical loading frame proposed by ISRM [29] and ASTM [32] for the Brazilian tension test employs curved or flat platens and is designed primarily for cylindrical rock discs, enabling diametral loading along the central axis of the specimen. However, block specimens are often preferred when investigating the shear and/or shear-flow behavior of rock joints, and these are not readily compatible with the standard loading frame. In such cases, a wedge-shaped loading frame is commonly adopted to accommodate block specimens and to implement a stress state comparable to that in the Brazilian test. The wedge-shaped loading frame was fabricated from hardened steel (Rockwell hardness higher than 58) for durability, and its loading faces contacted the specimen notches at 90°, accurately aligning the applied load with the loading axis. To maintain consistent boundary conditions across specimen types, the same wedge loading frame was used for cylindrical specimens.

Prior to testing, a pair of opposed notches was carefully machined at the designated loading parts on each specimen. Each notch was approximately 1 mm in depth and 1 mm in width, and the two notches were positioned 180° apart (diametrically opposite) to align the applied load with the central axis of the specimen. Careful setup and notch alignment with the central axis of the specimen were used to minimize experimental error; tests exhibiting obvious off-axis fracture were later excluded from the analyses (see Section 3).

The splitting tests were conducted using an MTS 816 rock testing system. For each test, a constant displacement rate was applied (0.01, 0.005, 0.001, 0.0005, and 0.0001 mm/s). During the test, the rock testing system measured axial load with a calibrated load cell and axial displacement with the built-in stroke LVDT (linear variable displacement transducer). Before each test, specimens were seated by applying a small preload to ensure full contact between the wedges and the notches. Angular misalignment was minimized by aligning the notch line with the loading axis. Fig. 2 illustrates the overall experimental setup for the splitting tests.

## 2.3 3D laser scanning

To quantify the geometric properties of rock joints, it is essential to accurately measure surface coordinates. Various techniques have been proposed to measure the joint surface. Among them, non-contact measurement using a laser scanner is one of the most widely applied techniques [33, 34]. In this study, a 3D laser line profile sensor (Gocator 2530) was used to acquire the coordinates of joint surfaces. The sensor provides a maximum lateral (x-axis) resolution of 28 μm and a vertical (z-axis) repeatability of 0.5 μm. By combining three sensors in parallel, it is possible to accommodate a field of view (FOV) ranging from 144 to 300 mm, thereby enabling a wider scanning area in a single run. Specimens were mounted on a motorized translation stage and traversed at a constant speed along the y-axis. A movement precision of 5 μm allows for the consistent and rapid acquisition of the target surface.

After splitting, each specimen was mounted on a V-block to ensure that the surface was positioned as close to horizontal as practicable. Then, the 3D laser scanner captured an area slightly larger than the joint surface to avoid edge truncation and minimize information loss. Regions outside the target joint surface were subsequently cropped during preprocessing to retain only the valid surface data. Exposure and gain were kept constant within a session, and loose debris was removed before scanning to prevent outliers.

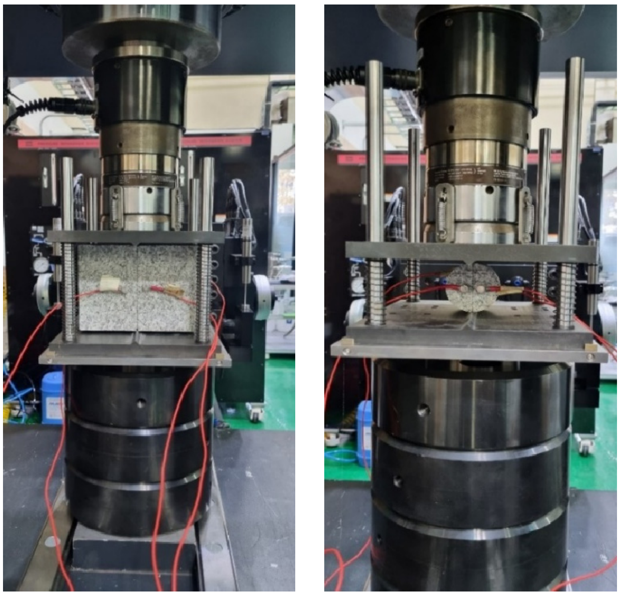

Figure 2. Experimental setup for wedge-splitting tests (MTS 816 rock testing system with wedge-shaped loading frame)

## 2.4 Preprocessing of joint surface data

Since the scanned raw data do not directly permit the computation of the geometric properties of the joints, preprocessing was required and applied as a standardized workflow: noise/boundary removal, detrending, surface alignment, overlap masking, and gridding.

(1) Noise and boundary removal (DBSCAN): The scanned surface was represented as a point cloud. Most points were densely sampled with small point spacing and corresponded to the surface of interest, whereas boundary regions or laser-scatter artifacts were sparser and more widely spaced, indicating potential outliers or irrelevant boundary data. In this context, DBSCAN (Density-Based Spatial Clustering of Applications with Noise) is well suited to automatically remove noise and redundant parts. DBSCAN is a density-based clustering algorithm widely used for data clustering and/or outlier detection [35]. Given a neighborhood radius and a minimum number of neighbors, points that are density-reachable from a core point are aggregated into clusters. Densely grouped points form major clusters, while sparse points are labeled as noise or appear as small clusters. In practice, the largest cluster typically corresponds to the valid joint surface, and the remaining clusters and noise can be discarded.

(2) Trimming: To mitigate boundary artifacts caused by concentrated loading and associated cracking, an additional 2.5% margin was trimmed from each edge of the retained cluster.

(3) Detrending: A best-fit regression plane, $z = ax + by + c$, was estimated by the least squares method and subtracted to remove possible trend that could bias morphology evaluation.

(4) Alignment of opposing surfaces: The opposing (upper and lower) surfaces were then aligned using the ICP (Iterative Closest Point) algorithm [36]. The ICP algorithm enhances the accuracy of a dataset by iteratively adjusting the orientation and position of the point clouds until the best possible degree of alignment is achieved.

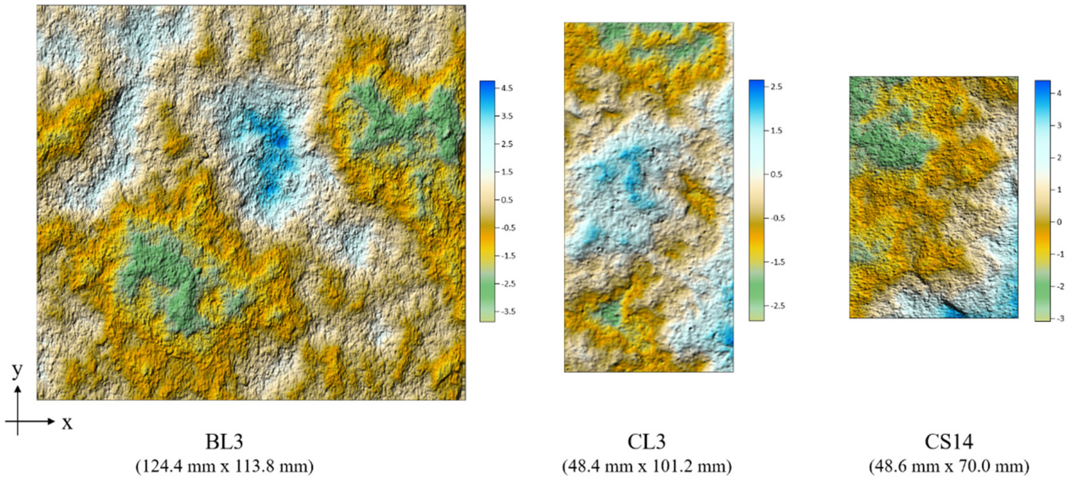


Figure 3. Processed joint surface topography after preprocessing (x: loading axis, y: perpendicular, z: elevation)

(5) Overlap masking: After achieving optimal alignment, non-overlapping regions were masked so that only the common overlap region was retained for analysis. This procedure avoids edge effects and ensures that directional profiles sample identical support.

(6) Gridding and interpolation: The overlap region was resampled onto a regular grid with a spacing of 0.1 mm across the entire joint surface.

(7) Coordinate convention: The axes were defined such that x is aligned with the loading axis, y is perpendicular to it, and z denotes surface elevation. This convention is used consistently in the directional analyses. Representative results of the preprocessing are shown in Fig. 3.

## 3. Evaluation of morphological characteristics

Out of the 45 prepared specimens, 36 (13 BL, 10 CL, and 13 CS) met the criteria and were retained for analysis. The discarded nine specimens commonly showed measurably off-axis relative to the loading direction, likely due to pre-existing micro-cracks or minor notch misalignment. Thus, those specimens were excluded from geometric analyses. Although this screening was necessary to ensure consistent directional and comparative analyses, the unequal number of discarded specimens among groups, particularly in the CL group, may have reduced the statistical balance of the dataset. Therefore, for directional roughness evaluation, each directional value was obtained from multiple parallel profiles, with at least seven profiles extracted for a given direction in each specimen so as to complement the balance of dataset. As a result, the representative roughness value was calculated from their arithmetic mean.

Prior to scanning, loose rock powder and debris was removed to prevent measurement error. Joint surfaces were digitized and preprocessed as described in Sections 2.3~2.4. Morphological characterization targeted two complementary viewpoints, i.e., roughness and the spatial correlation of surface elevation.

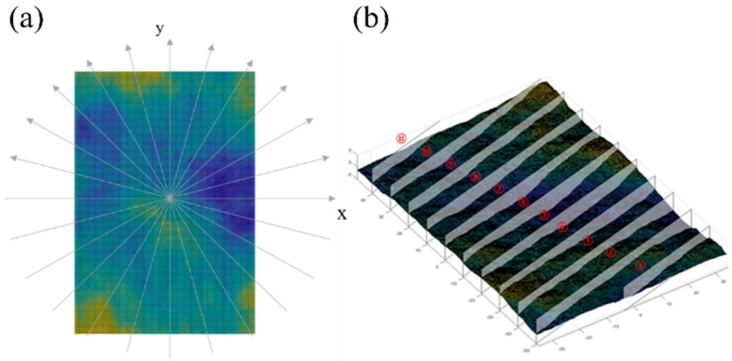


Figure 4. Method for directional roughness estimation; (a) axis assignment (x: loading axis, y: perpendicular), and (b) rotating sampling (θ advanced counterclockwise in 15°)

### 3.1 Roughness parameters and directional evaluation

The roughness of a rock joint significantly influences the THM behavior of rock masses so that various roughness parameters have been proposed. Among these, the JRC (Joint Roughness Coefficient) is one of the most representative and widely adopted parameters [37]. Despite its widespread use, JRC, like many other roughness parameters, has inherent limitations. Likewise, no single parameter has been recognized as universally suitable for all perspectives. Consequently, applying multiple and complementary roughness parameters is recommended for a comprehensive roughness assessment [38].

This study applied three different roughness parameters to capture distinct aspects of joint surface morphology. The first is the CLA (Center Line Average), which quantifies overall amplitude as the mean absolute deviation of a profile from its mean line, thereby providing a direct measure of vertical variability along the center line [39]. It is conceptually related to other parameters, such as the roughness profile index [40], and the ultimate slope of the profile [41]. The second parameter, Z2, is the root mean square (RMS) of the first derivative of a profile [42]. It mainly emphasizes micro-asperities and the local slope of the surface. Parameters similar to Z2 include the average inclination angle of asperities and the standard deviation of the asperity angle [40]. Eqs. (1) and (2) show the definitions of CLA and Z2, respectively.

$$CLA = \frac{1}{L}\int_0^L |y|dx = \frac{1}{L}\sum_{i=1}^{n-1}|y_i|\Delta x \tag{1}$$

$$Z2 = \sqrt{\frac{1}{L}\int_0^L \left(\frac{dy}{dx}\right)^2 dx} = \sqrt{\frac{1}{L}\sum_{i=1}^{n-1}\frac{(y_{i+1}-y_i)^2}{x_{i+1}-x_i}} \tag{2}$$

The last parameter is the fractal dimension. Since Mandelbrot [43], the study of rock joint geometry using fractal concepts has been a consistent research topic. Under the assumption that joint surfaces are self-affine, various studies have measured fractal properties or numerically generated profiles or surfaces with specific characteristics. In this study, the fractal dimension of the joint surfaces was evaluated using an FFT-based spectral method. Joint profiles extracted from the surface were transformed into the frequency domain to obtain the power spectral density, and the slope (β) in log-log space was determined by linear regression over the scale invariant range. Once the slope of the regression line was calculated, the Hurst exponent (H) was determined as shown in Eq. (3) for a joint profile. The fractal dimension (D) is then related to the Hurst exponent by the relationship, D = 2 – E for a profile and D = 3 – H for a surface.

$$H = \frac{-\beta - 1}{2} \tag{3}$$

where E is the Euclidean dimension.

The aforementioned 2D parameters may not fully capture the characteristics and directionality of a joint surface, which is inherently 3D. Therefore, we adapted the workflow to quantify directional roughness (Fig. 4).

First, as shown in Fig. 4(a), the longer side of the scanned area was assigned to the y-axis. Next, as illustrated in Fig. 4(b), a slicing plane was rotated counterclockwise in 15° increments from the x-axis (0° reference) to 165°, and for each angle a family of parallel cross-sections was extracted. The three roughness parameters (CLA, Z2, and D) were then computed for each profile set. Finally, for each direction, the distribution of each parameter was summarized in a histogram, and the arithmetic mean (taken as the representative roughness value) and standard deviation were calculated for that specific direction.

## 3.2 Spatial correlation

Spatial correlation, which describes the similarity of a property as a function of lag distance, is an important concept in geostatistics and can be quantified by several methods, including the variogram, madogram, and autocorrelation. In this study, we adopted the (semi)variogram and the basic formulation is shown in Eq. (4).

$$\gamma(h) = \frac{1}{2n}\sum_{i=1}^{n}[z(x_i) - z(x_i + h)]^2 \tag{4}$$

where $x_i$ is a specific location, $h$ is the lag distance, and $z(x_i)$ is the value of property at location $x_i$.

Variograms provide a measure of how data similarity changes with separation distance, making them useful in many engineering and geological applications. Various studies have utilized the variogram to analyze the spatial correlation of joint surfaces and/or aperture [44-46], and to establish quantitative relationships between the variogram and joint roughness [47-49]. In this study, we evaluated the spatial correlation of joint surface elevation.

To facilitate the analysis, the experimental variogram was constructed on a polar grid with an angular division of 180° and a radial division of 100 segments so as to ensure adequate spatial coverage. Variogram anisotropy was investigated by rotating the lag vector in 15° counterclockwise increments with an angular tolerance of ±5°. After computing the experimental variogram under the defined settings, a theoretical variogram model was fitted. In most cases, the spherical model (Eq. (5)) provided a sufficiently appropriate representation.

$$\gamma(h) = \begin{cases} C_0 + C\left[1.5\left(\frac{h}{a}\right) - 0.5\left(\frac{h}{a}\right)^3\right] & h \le a \\ C_0 + C & h > a \end{cases} \tag{5}$$

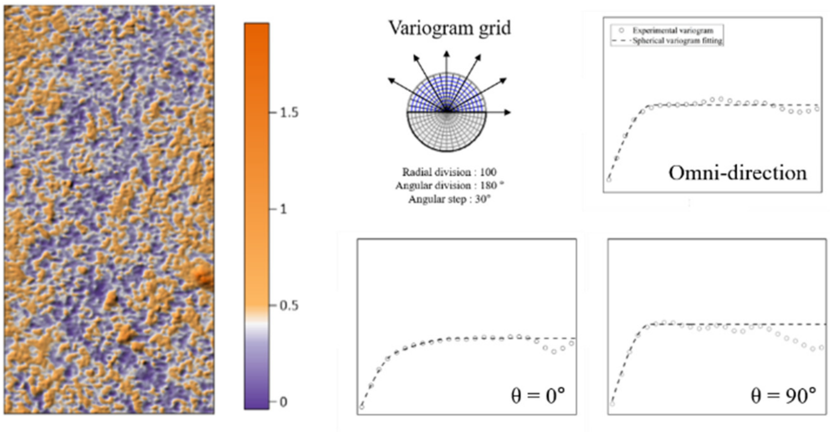


Figure 5. Procedure of calculating spatial correlation based on variogram

where $C_0$ is the nugget, $C$ is the partial sill, and $a$ is the range.

Theoretical model fitting was conducted mainly based on variogram points at lags up to the first peak. Data outside this peak were considered less important, since the main purpose was to examine variations in the fitted variogram parameters. Fig. 5 shows an example of the variogram analysis. We focused on two main variogram parameters, i.e., the range and the sill, and their dependence on the experimental factors. Anisotropy in range and sill was evaluated at 15° angular increments, and an omni-directional variogram was also analyzed. We estimated the nugget jointly with the range and sill, but when the estimated nugget was statistically indistinguishable from zero, it was assigned as zero.

## 4. Results and discussion

### 4.1 Joint roughness

#### 4.1.1 Effect of loading rate

Fig. 6 shows the variation of the three roughness parameters with loading rate. Although roughness was evaluated for various directions as described in Fig. 4, only the results for θ = 0° (parallel to the loading direction) and θ = 90° (perpendicular to the loading axis) are presented in Fig. 6 for brevity.

The CLA, which reflects the overall amplitude of the joint, ranged from 0.51 to 0.93. The Z2, which emphasizes micro-asperities, ranged from 0.27 to 0.41, and the fractal dimension ranged from 1.42 to 1.68. Across the tested loading rates, none of the three parameters exhibited a consistent dependence on the loading rate, despite their representing different aspects of surface morphology. Some previous studies have reported specific trends regarding loading rate effects, however, the available literature is not fully consistent. For example, Shams et al. [26] reported rougher joints at lower loading rates in granite under Brazilian splitting and Babadagli and Develi [24] reported a loading rate dependent trend in fractal dimension for tensile joints. By contrast, Backers et al. [50] reported that joint surface roughness remained essentially unchanged over the

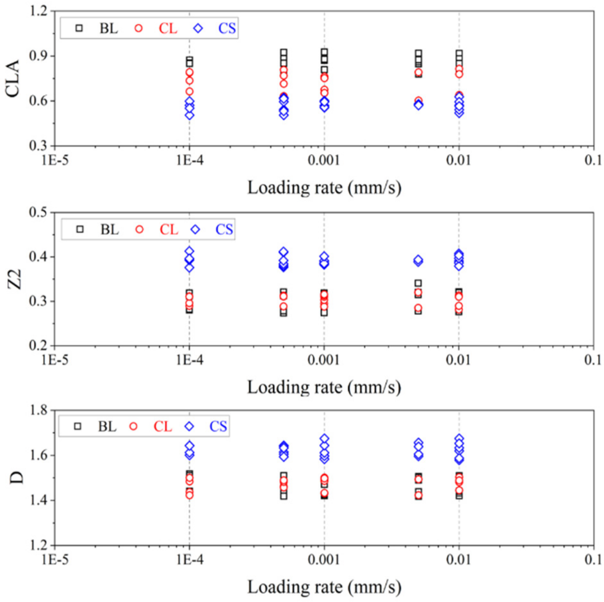


Figure 6. Variation of each roughness parameter according to the loading rate (0.0001~0.01 mm/s)

tested loading rate range in mode I fracture experiments on sandstone. Although the experimental conditions of Backers et al. [50], including lithology, fracture mode, and loading configuration, differ from those of the present study, their results still suggest that the influence of loading rate on joint morphology is not necessarily universal. Taken together, these observations indicate that the loading rate dependence of joint morphology may vary with many factors, such as lithology, specimen geometry, and selected roughness parameters as well as the experimental factors considered in this study. Therefore, the absence of a clear loading rate dependence is interpreted within the context of the present experiments, rather than as a simple contradiction of previous studies. Meanwhile, differences in roughness levels among specimen types were also observed, and these are discussed in the following section.

#### 4.1.2 Effect of specimen size

Fig. 7 shows the results for the three roughness parameters, grouped by BL, CL, and CS. Additionally, the descriptive statistics for each parameter according to specimen size are summarized in Table 2.

As it can be seen in Fig. 7, the CLA increased with specimen size. Due to their composite mineralogy and complex geological process, rocks inherently contain internal micro-discontinuities, including micro-cracks, pores, and mineral grain boundaries. As specimen size increases, the number of such discontinuities contained within a specimen also increases. Under load, fracturing tends to propagate along these pre-existing discontinuities. In larger specimens, the crack is more likely to intersect and coalesce with a greater number of these features, plausibly producing a larger overall amplitude on the resulting joint surface. In addition, larger specimens accumulate greater strain energy prior to failure. This elevated energy accumulation can induce a more brittle fracturing response, which may further contribute to the observed increase in CLA.

Table 2. Descriptive statistics of roughness parameters according to the specimen size (BL, CL, and CS specimen)

| | | Average | Standard deviation | Min | Max |
|---|---|---|---|---|---|
| CLA | BL | 0.85 | 0.04 | 0.78 | 0.92 |
| | CL | 0.71 | 0.09 | 0.56 | 0.81 |
| | CS | 0.56 | 0.04 | 0.49 | 0.63 |
| Z2 | BL | 0.29 | 0.02 | 0.27 | 0.32 |
| | CL | 0.31 | 0.01 | 0.29 | 0.32 |
| | CS | 0.40 | 0.01 | 0.38 | 0.41 |
| D | BL | 1.46 | 0.03 | 1.42 | 1.52 |
| | CL | 1.48 | 0.02 | 1.42 | 1.50 |
| | CS | 1.61 | 0.03 | 1.58 | 1.68 |

In contrast, for Z2, the BL and CL specimens showed comparable roughness values. However, the smallest specimens (CS) exhibited a relatively higher roughness. Possible causes for this observed tendency are as follows. First, a reduction in specimen size decreases the number of internal micro-cracks and pores. Consequently, their influence on the overall fracturing behavior may be reduced. This can result in a more localized fracturing mechanism, characterized by intra-granular or inter-granular failure, which increases local slopes and thus increases Z2. Furthermore, a decrease in specimen size can amplify the influence of internal heterogeneity, specifically the effects of certain individual minerals and pre-existing cracks, potentially resulting in an increase in microscale roughness within smaller regions. Additionally, the shorter profile length in CS specimens reduces the spatial averaging of steep asperities, which can affect parameters such as Z2.

A comparable trend was also observed for the fractal dimension (D), similar to that of Z2. While the BL and CL specimens exhibited comparable D values, the smallest specimens (CS) showed higher D (i.e., greater small scale roughness). As the observation scale decreases, small scale unevenness of the joint surface becomes more influential than waviness. This is consistent with the findings for Z2, because Z2 emphasizes local slope and micro-asperities. This enhanced small scale irregularity plausibly increases the estimated fractal dimension. The combined results of CLA, Z2, and D show that size effects on fracture surface morphology are parameter dependent, reflecting the multiscale and heterogeneous feature of wedge-splitting fracture.

To assess whether the observed differences among size groups were statistically meaningful, one-way ANOVA was applied to each roughness parameter at a significance level of 0.05, and Scheffe's post-hoc test was used for pairwise comparisons when the overall group effect was significant. Under this framework, CLA and Z2 both showed significant differences among all three groups, whereas for fractal dimension the CS group differed significantly from both BL and CL, while BL and CL did not differ significantly from each other. These results support the interpretation that the size effect is parameter-dependent rather than uniform across all descriptors.

The size dependent results reveal a bifurcated response of joint morphology. The CLA increased with specimen size, consistent with larger specimens sampling more pre-existing micro-discontinuities and storing more strain energy prior to failure, both of which promote greater out-of-plane amplitude. In contrast, slope and scale sensitive measures are elevated in the smallest specimens. Z2 and D are relatively higher for CS than BL and CL, indicating that micro-scale or short wavelength asperities dominate at smaller scale. Overall, specimen size governs which scale

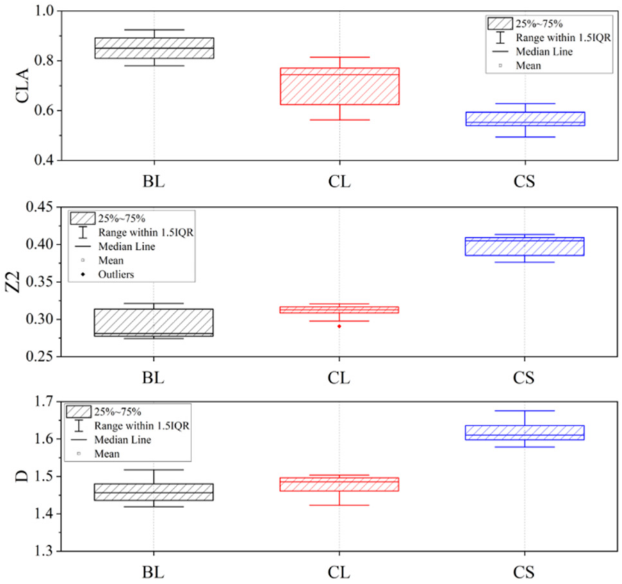

Figure 7. Variation of roughness parameters according to the specimen size (BL, CL, and CS specimen)

of roughness is emphasized, i.e., long wavelength (waviness) in larger specimens and short wavelength (unevenness) in smaller specimens. This highlights the multiscale feature of wedge-splitting surfaces.

Meanwhile, Vogler et al. [11] compared the surface properties of natural and artificially generated joints and analysed the relationship between specimen size and roughness for the artificial joints. After creating artificial tensile joints using the Brazilian test, their analysis using Z2 and the standard deviation of the surface height indicated that roughness decreased as specimen size decreased. Except for CLA, the trends for Z2 and D observed in the present study were contrary to their findings, with CS exhibiting higher micro-scale roughness. Notably, CS groups also showed the greatest variability. These discrepancies may reflect differences in the loading configuration and resulting stress state (wedge-splitting with notches versus diametral Brazilian loading), as well as the potential influence of lithology and specimen shape. The discrepancy with Vogler et al. [11] may be interpreted more specifically in terms of the fracture generation mechanism. Their Brazilian based artificial joints tended to become smoother as specimen size decreased, which they related to size-dependent tensile stress conditions and the resulting crack path. By contrast, the present tests with opposed notches yielded relatively higher Z2 and D in the smallest specimens, suggesting that smaller specimens under the present configuration may preserve more localized, short wavelength asperities. Therefore, the difference from previous studies is not interpreted here as a simple contradiction, but rather as evidence that the apparent size effect on joint roughness depends on how the tensile joint is generated and on the scale of roughness is emphasized by the selected parameter.

In this study, a pair of diametrically opposed notches was created at the specimen center to generate a tensile joint, and loading was applied with a wedge-shaped frame. This configuration likely produces a stress state that differs from that of the conventional Brazilian test. Fig. 8 presents the relationship between loading rate and failure strength, calculated from the measured

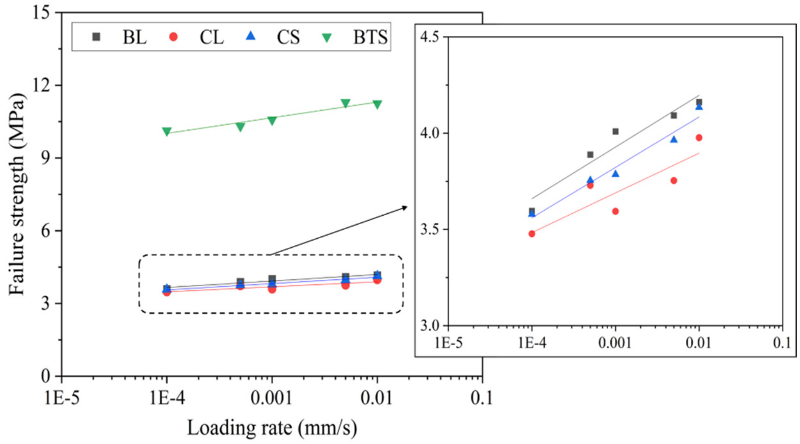


Figure 8. Apparent strength from wedge-splitting test and comparison with the conventional Brazilian tensile strength

peak load during the splitting tests. The failure strength was calculated as the apparent strength, simply defined as the peak load at failure divided by the joint surface area. For comparison, conventional Brazilian tests were also conducted on the Hwangdeung granite in accordance with the ISRM suggested method [29], and the two sets of results are shown in Fig. 8.

As shown in Fig. 8, the apparent tensile strength obtained from the wedge-splitting test was approximately 1/4 to 1/3 of the Brazilian tensile strength. While this may be partly attributable to use of a simple apparent strength definition that does not explicitly account for the effect of the notch, it also suggests that the stress state and resulting cracking mechanism may differ from those of a conventional Brazilian test. Differences in loading configuration likely influenced both the measured strength and the specimen size effect on surface roughness, potentially explaining the differences from previous research.

In fracture mechanics, the wedge-shaped loading configuration is often adopted to measure relevant properties, i.e., fracture toughness and/or specific fracture energy. One of the strengths of this configuration is its ability to control splitting of a specimen and transfer load stably through the prefabricated notch, thereby promoting stable crack propagation [51]. It is similar to the present experimental setup, although it was not introduced here to reproduce a standard fracture mechanics test, but rather to accommodate block specimens. In this respect, the present configuration differs from the conventional Brazilian test. In Brazilian configuration, tensile failure develops through diametral compression and an indirect tensile stress field within the specimen [52]. Although it is a standardized method for the indirect measurements of tensile strength, it is less suitable for investigating cracking behavior, particularly the cracking mechanism and crack initiation location [53, 54]. In contrast, wedge-contact loading with prefabricated notches is associated with a more localized and guided crack initiation process, leading to more stable cracking propagation. Therefore, the stress development and fracture process in the present tests may differ from those of the Brazilian test, which can lead to both lower apparent strength and different fracture surface morphology. Although a rigorous stress analysis is beyond the scope of this study, the present results indicate that the adopted configuration should be interpreted as a practical method for controlled artificial joint generation, rather than as mechanically identical to the conventional Brazilian test.

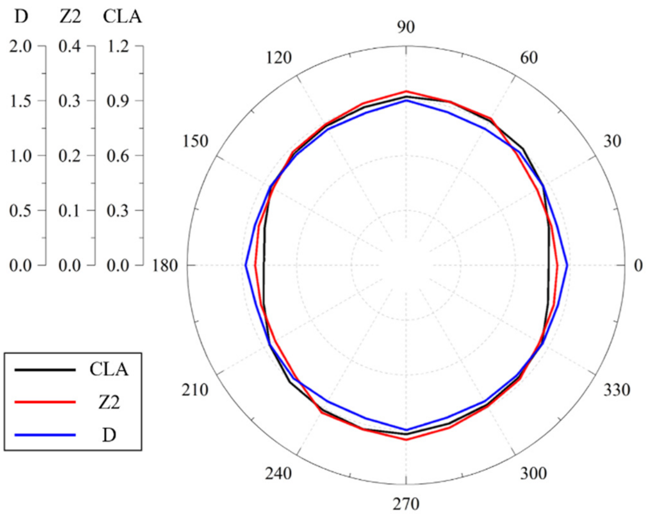


Figure 9. Directional roughness (example, BL specimen) in polar distribution

#### 4.1.3 Effect of loading direction

Several studies have investigated the anisotropy of joint roughness, by generating 2D profiles along various directions [18, 55]. In the present study, directional roughness was evaluated at 15° intervals, following the methodology detailed in Fig. 4. An example of the directional roughness is provided in Fig. 9.

In Fig. 9, the distributions of the three parameters are approximately elliptical, but the overall anisotropy (quantified by the maximum to minimum ratio) is modest (with ratios of 1.19 for CLA, 1.16 for Z2, and 1.06 for D, respectively). Examination of all 36 joint surfaces across all directions indicated that it is difficult to draw a generalized conclusion. Nevertheless, several features were consistently observed in most cases, as described below.

The loading direction during the splitting test significantly affected the roughness of the artificial tensile surfaces. This is corroborated in Fig. 10, which reorganizes the data from Fig. 7 according to the two principal directions (θ = 0° and 90°).

The CLA showed higher values in the direction perpendicular to the loading axis than in that parallel to the loading axis. This trend was more pronounced for specimens with shorter lengths in the loading direction (i.e., it was more evident in CL and CS than in BL), suggesting that the specimen geometry influences amplitude-based roughness. The Z2 likewise showed greater roughness in the perpendicular than in the parallel direction, which was a consistent pattern across all specimen types, indicating an effect of stress direction on the asperity-level features of the split surface. The fractal dimension was also higher in the perpendicular regardless of specimen type. However, its anisotropy ratio was relatively smaller than those of CLA and Z2. Descriptive statistics for the two principal directions are summarized in Table 3.

To evaluate directional effects, the values at θ = 0° and 90° were compared within each specimen type, because both directional values were derived from the same specimen. At the 0.05 significance level, significant directional differences were found for all roughness parameters

Table 3. Descriptive statistics of roughness parameters along the two primary directions (θ = 0° and 90°)

| | | | Average | Standard deviation | CV (%) |
|---|---|---|---|---|---|
| CLA | BL | θ = 0° | 0.8517 | 0.0462 | 5.42 |
| | | θ = 90° | 0.8561 | 0.0318 | 3.71 |
| | | Ratio | 1.01 | - | - |
| | CL | θ = 0° | 0.6366 | 0.0742 | 11.66 |
| | | θ = 90° | 0.7769 | 0.0237 | 3.06 |
| | | Ratio | 1.22 | - | - |
| | CS | θ = 0° | 0.5347 | 0.0265 | 4.97 |
| | | θ = 90° | 0.5873 | 0.0328 | 5.59 |
| | | Ratio | 1.10 | - | - |
| Z2 | BL | θ = 0° | 0.2783 | 0.0028 | 1.02 |
| | | θ = 90° | 0.3163 | 0.0035 | 1.09 |
| | | Ratio | 1.14 | - | - |
| | CL | θ = 0° | 0.3019 | 0.0094 | 3.11 |
| | | θ = 90° | 0.3152 | 0.0039 | 1.23 |
| | | Ratio | 1.04 | - | - |
| | CS | θ = 0° | 0.3855 | 0.0053 | 1.39 |
| | | θ = 90° | 0.4073 | 0.0068 | 1.66 |
| | | Ratio | 1.06 | - | - |
| D | BL | θ = 0° | 1.4318 | 0.0083 | 0.58 |
| | | θ = 90° | 1.4859 | 0.0138 | 0.92 |
| | | Ratio | 1.04 | - | - |
| | CL | θ = 0° | 1.4590 | 0.0244 | 1.67 |
| | | θ = 90° | 1.4918 | 0.0067 | 0.45 |
| | | Ratio | 1.02 | - | - |
| | CS | θ = 0° | 1.6007 | 0.0126 | 0.79 |
| | | θ = 90° | 1.6558 | 0.0154 | 0.93 |
| | | Ratio | 1.03 | - | - |

except for CLA in the BL group. The direction of the difference was also consistent in most cases: roughness was greater at θ = 90° than at θ = 0°, indicating that the anisotropy observed in the descriptive statistics is supported by the comparisons.

All the specimens used in this study showed no noticeable anisotropy in terms of mineral arrangement or texture. Accordingly, we considered the intact rock matrix to be isotropic and assumed that minerals and pre-existing micro-cracks were randomly distributed. Despite these overall isotropic features, the mechanical response under the specific loading conditions showed clear directional dependence. It is well known that crack initiation and propagation generally follow the direction of the applied stress. Therefore, cracks tend to propagate and coalesce with a certain degree of continuity along the loading direction (the x-axis in Fig. 4), producing comparatively smoother relief in the parallel direction. In contrast, in the direction perpendicular to the loading axis, the split surfaces exhibit more irregular topography. This likely reflects the lower resolved tensile component in that direction, which allows local heterogeneity (mineral contrasts and micro-cracks) to exert a stronger influence and yield a more heterogeneous cracking pattern.

The directional tendency is broadly consistent with previous studies showing that roughness anisotropy depends on both loading direction and specimen geometry [27]. The present results further suggest that, under wedge-splitting, the direction perpendicular to the loading axis is more

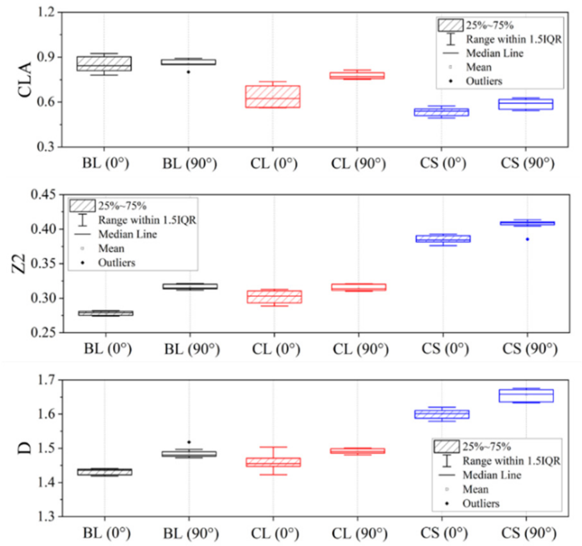


Figure 10. Variation of roughness parameters in the two principal directions (θ = 0° and 90°)

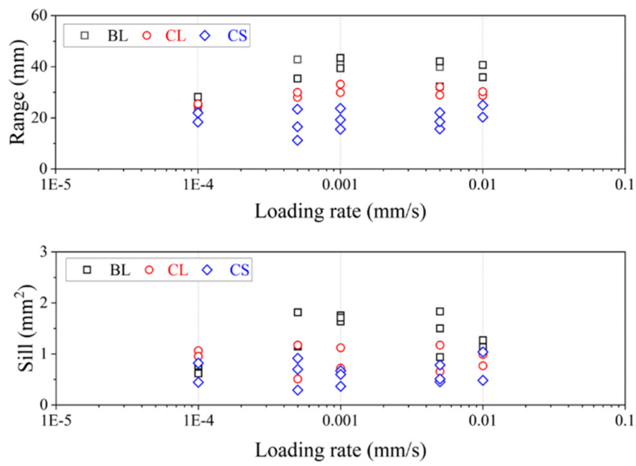


Figure 11. Variation of each variogram parameter according to the loading rate (0.0001~0.01 mm/s)

likely to preserve irregular topography, whereas the parallel direction tends to reflect a smoother and more continuous crack path. Accordingly, directional roughness should be interpreted in relation not only to material heterogeneity but also to the boundary and loading conditions used to generate the joint.

### 4.2 Spatial correlation of the surface elevation

#### 4.2.1 Effect of loading rate

Fig. 11 shows the variation of the two main variogram parameters according to the loading rate. The results were obtained from omni-directional modelling, without accounting for directionality.

The variogram range spanned approximately 11~43 mm, and the sill ranged 0.3~1.8 $mm^2$. Similar to the roughness variation, no distinct correlation between loading rate and either parameter was identified. Therefore, within the loading rate range applied in this study, we found no morphological differences in Hwangdeung granite. By contrast, some correlation with specimen type was noted; a detailed analysis is provided in the following section.

### 4.2.2 Effect of specimen size

Fig. 12 shows the results for the two variogram parameters according to the specimen size. In addition, the descriptive statistics are summarized in Table 4. The results were obtained from omni-directional modelling, which pools all directions and does not explicitly account for directionality

The variogram range increased with increasing specimen size. Likewise, the sill exhibited a corresponding increase with size. The observed increase can be explained by enhanced waviness as larger specimens intersect and coalesce with more pre-existing heterogeneities, thereby elevating overall variance (sill) and extending the distance over which elevations remain correlated (range).

The sill represents the plateau (i.e., maximum variance) of the variogram, that is, the total variance of the data once spatial correlation is lost. Because the sill scales with overall amplitude, a larger amplitude implies that the surface elevations are distributed over a wider range, which, in turn, yields a larger data variance and a greater sill. It is consistent with the experimental results: comparing the sill distribution in Fig. 12 with the CLA trend in Fig. 6 reveals a coherent pattern, indicating a positive relationship between the sill and CLA.

Micro-asperities are related to the nugget effect. The nugget corresponds to the variogram variance at zero separation distance (or extrapolated to that point) and represents the inherent variability of data and potential measurement noise. In this study, nugget estimates from the fitted spherical model (Eq. (5)) were generally near zero or showed no consistent trend; therefore, they are not reported.

The variogram range signifies the maximum separation distance over which spatial correlation persists. It is difficult to establish a direct relationship between the range and the other roughness parameters used in this study. However, previous research has shown that the initial slope of the variogram curve is related to joint roughness, and in some cases, roughness parameters have been proposed using this relationship [45, 47, 48]. Accordingly, we estimated the variogram slope from the fitted spherical model in Fig. 12. For a spherical model, the initial slope is $(d\gamma/dh)|_{h\to 0} = 1.5(c/a)$, where $c$ is the sill and $a$ is the range. In addition, it was calculated in the form of $\sqrt{c}/a$ so as to normalize the slope into a dimensionless form. The average slope for the BL, CL, and CS specimens was 0.0313, 0.0328, and 0.0406, respectively, which is consistent with the trends observed for Z2 and D in Fig. 6. In summary, we find a qualitative correlation between the sill and CLA, and a corresponding association between the normalized initial variogram slope and Z2 and D.

To test whether the variogram parameters differed systematically with specimen size, one-way ANOVA was applied at a significance level of 0.05, followed by Scheffe's post-hoc test where the overall group effect was significant. The range showed a significant overall difference across the three specimen groups, indicating a clear size dependence in spatial correlation length. For the sill, significant differences were observed only in comparisons involving the BL group, whereas the CL and CS groups were not significantly different from each other. This result suggests that the size effect is more robust for correlation length than for elevation variance.

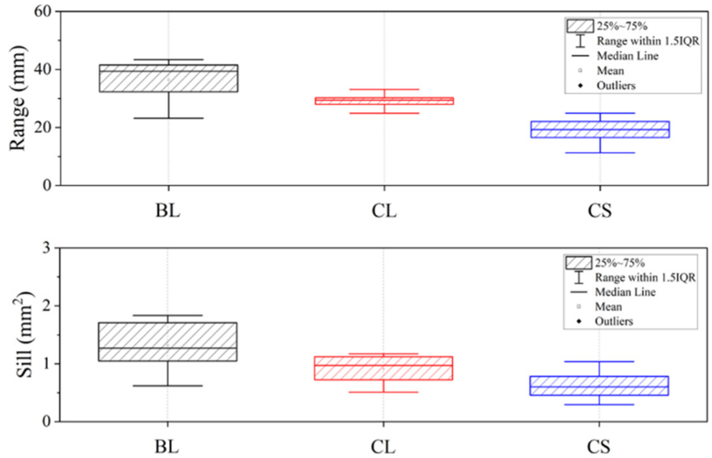


Figure 12. Variation of variogram parameters according to the specimen size (BL, CL, and CS specimen)

Table 4. Descriptive statistics of variogram parameters according to the specimen size (BL, CL, and CS specimen)

| | | Average | Standard deviation | Min | Max |
|---|---|---|---|---|---|
| Range (mm) | BL | 36.46 | 6.21 | 23.19 | 43.40 |
| | CL | 29.14 | 2.46 | 24.89 | 33.13 |
| | CS | 19.35 | 3.78 | 11.25 | 24.97 |
| Sill ($mm^2$) | BL | 1.32 | 0.40 | 0.62 | 1.83 |
| | CL | 0.91 | 0.22 | 0.51 | 1.17 |
| | CS | 0.62 | 0.21 | 0.29 | 1.04 |

The adopted morphology parameters reflect different physical scales of joint surface geometry. CLA and the variogram sill mainly represent overall amplitude or variance, Z2 emphasizes local slope and micro-asperities, D reflects small-scale irregularity, and the variogram range represents spatial correlation length. Accordingly, the specimen size effect observed in this study is parameter-dependent: larger specimens emphasize large-scale waviness and longer correlation length, whereas smaller specimens more strongly preserve short-wavelength asperities and local slope. This explains why CLA, sill, and range increase with specimen size, while Z2 and D show relatively higher values in the smallest specimens.

### 4.2.3 Effect of loading direction

Similar to the directional roughness analysis, we first calculated directional variograms at designated angular intervals; however, no consistent trend was discernible. Consequently, the variogram parameters were evaluated along the two principal directions defined by the loading axis (θ = 0° and 90°). The distributions of these values are illustrated as box charts in Fig. 13, and their descriptive statistics are summarized in Table 5.

Unlike the roughness directionality with respect to the loading direction, the variogram range did not show a consistent directional trend across specimen types. In the CL and CS specimens, a larger range was measured at θ = 90°, whereas the opposite trend was observed for the BL

Table 5. Descriptive statistics of variogram parameters along the two primary directions (θ = 0° and 90°)

| | | | Average | Standard deviation | CV (%) |
|---|---|---|---|---|---|
| Range (mm) | BL | θ = 0° | 37.2860 | 6.1801 | 16.57 |
| | | θ = 90° | 35.2648 | 4.1288 | 11.71 |
| | | Ratio | 0.95 | - | - |
| | CL | θ = 0° | 23.3642 | 2.2717 | 9.72 |
| | | θ = 90° | 28.6385 | 4.3566 | 15.21 |
| | | Ratio | 1.23 | - | - |
| | CS | θ = 0° | 18.9138 | 5.4961 | 29.06 |
| | | θ = 90° | 18.8552 | 4.3481 | 23.06 |
| | | Ratio | 1.00 | - | - |
| Sill ($mm^2$) | BL | θ = 0° | 1.2630 | 0.4379 | 34.67 |
| | | θ = 90° | 1.2890 | 0.3836 | 29.76 |
| | | Ratio | 1.02 | - | - |
| | CL | θ = 0° | 0.7965 | 0.0762 | 9.57 |
| | | θ = 90° | 1.0244 | 0.2824 | 27.57 |
| | | Ratio | 1.29 | - | - |
| | CS | θ = 0° | 0.5331 | 0.1975 | 37.05 |
| | | θ = 90° | 0.6659 | 0.2829 | 42.48 |
| | | Ratio | 1.25 | - | - |

specimens. By contrast, the sill consistently showed larger values at θ = 90° across all specimen types. As noted above, because the sill correlates with overall surface amplitude, this pattern is similar to the CLA distribution in Fig. 9. However, the sill values displayed relatively larger dispersion than the roughness parameters, indicating a greater variability in the variogram-based estimates.

Directional differences in variogram parameters were evaluated between the two principal directions within each specimen type. At the 0.05 significance level, most comparisons were not statistically significant, the only exception being the range of the CL specimens. That is, anisotropy in the fitted variogram parameters is generally weak and less systematic than that observed in the roughness parameters. This difference arises because roughness and variogram parameters reflect different morphological aspects. Roughness parameters are more sensitive to directional differences in amplitude, local slope, and small-scale irregularity, whereas variogram parameters mainly describe broader spatial continuity and correlation length. In particular, the sill showed a directionally similar tendency to CLA because both are influenced by overall amplitude, whereas the range reflects correlation length and therefore did not show a comparably consistent directional response. In addition, because the variogram parameters were obtained through model fitting and displayed relatively larger dispersion than the roughness, directional tendencies may appear less distinct in the statistical comparisons

### 4.3 Limitations and future study

Although wedge-splitting provides a reproducible and practical method for generating artificial tensile joints, the resulting surfaces should not be regarded as exact equivalents of natural joints, which are formed under far more complex geological processes. Nevertheless, split artificial joints have been widely adopted in previous experimental studies as practical alternatives when reproducibility and control of test conditions are required. Therefore, the purpose of this study was not to reproduce the full formation mechanism of natural joints, but to systematically characterize the morphology of wedge-splitting based artificial joints and to examine the influence of major experimental factors under controlled conditions. The present findings should thus be interpreted within the scope of artificial tensile joints.

Despite this limitation, wedge-splitting offers clear advantages for comparative experimental studies because it allows repeatability and systematic variation of test variables. Future studies are recommended to further assess the representativeness of wedge-splitting joints through comparative evaluation with a wider range of natural joints. Additional investigation into the role of the stress state and the fracture propagation mechanism in shaping joint morphology would also help the improve interpretation of the present results and clarify the broader applicability of artificial joints.

From an engineering perspective, the morphology parameters obtained in this study may also provide useful reference data for subsequent mechanical, hydraulic, and coupled THM analyses of artificial rock joints. Roughness parameters such as CLA, Z2, and D quantify different aspects of surface morphology, including overall amplitude, local slope, and small-scale irregularity, whereas variogram parameters such as the sill and the range describe the variance and spatial continuity of surface elevation. Future work may therefore extend the present results by linking these morphology parameters more directly to joint contact behavior, shear response, aperture structure, fluid flow, and coupled THM processes through dedicated experiments and numerical modelling.

## 5. Conclusions

The characterization of rock joints is critical to many engineering applications and has therefore been the subject of extensive research. Because of practical limitations in testing natural joints or their replicas, artificially created joints produced by splitting intact rock are frequently adopted as a practical alternative. In this context, the present study provided an integrated characterization of wedge-splitting artificial tensile joints by evaluating roughness and spatial correlation together under a single experimental framework. The results showed that the morphological response of split joint surfaces is parameter and scale dependent, which helps explain why previous studies have not always reported consistent trends. The main conclusions are as follows.

- Within the tested range (0.0001~0.01 mm/s), the loading rate did not affect the morphological characteristics of the resulting joint surfaces in medium- to coarse-grained granite. This conclusion is supported by both the roughness and variogram parameters.
- Size dependent differences in roughness were parameter-specific. The amplitude-based parameter (CLA) was positively associated with specimen size, while micro-asperity-based (Z2) and the fractal dimension (D) exhibited negative relationships.
- A clear directional effect was observed in the roughness of the split joint surfaces with respect to the loading axis. Specifically, under wedge-splitting, greater roughness was consistently measured in the direction perpendicular to the applied load than in parallel, regardless of the type of parameter used.

- Variogram parameters increased with specimen size. Both the range and the sill were larger for bigger specimens. In contrast to the roughness results, directional differences in spatial correlation with respect to the loading axis were not pronounced and were generally not statistically significant.
- Consistent with the roughness analysis, the sill tracked CLA, and a normalized initial variogram slope aligned with Z2 and D, supporting a multiscale interpretation of the size effect.
- As contextual evidence, wedge-splitting yielded apparently lower strength than Brazilian tension tests, implying a different stress state; this may explain differences from other studies and motivates future work.

## Acknowledgements

The work was supported by the Institute for Korea Spent Nuclear Fuel (iKSNF) and National Research Foundation of Korea (NRF) grant funded by the Korea government (Ministry of Science and ICT, MSIT) (RS-2021-NR056198).

## References

1. Barton, N., Bandis, S., Bakhtar, K. (1985). Strength, deformation and conductivity coupling of rock joints. International Journal of Rock Mechanics and Mining Sciences & Geomechanics Abstracts, 22(3), 121-140. https://doi.org/10.1016/0148-9062(85)93227-9.
2. Olsson, R., Barton, N. (2001). An improved model for hydromechanical coupling during shearing of rock joints. International Journal of Rock Mechanics and Mining Sciences & Geomechanics Abstracts, 38(3), 317-329. https://doi.org/10.1016/S1365-1609(00)00079-4.
3. Grasselli, G., Egger, P. (2003). Constitutive law for the shear strength of rock joints based on three-dimensional surface parameters. International Journal of Rock Mechanics and Mining Sciences, 40, 25-40. https://doi.org/10.1016/S1365-1609(02)00101-6.
4. Rutqvist, J., Stephansson, O. (2003). The role of hydromechanical coupling in fractured rock engineering. Hydrogeology Journal, 11, 7-40. https://doi.org/10.1016/s10040-002-0241-5.
5. Zhao, L.H., Cao, J., Zhang, Y., Luo, Q. (2015). Effect of hydraulic distribution on the stability of a plane slide rock slope under the nonlinear Barton-Bandis failure criterion. Geomechanics and Engineering, 8(3), 391-414. https://doi.org/10.12989/gae.2015.8.3.391.
6. Galindo, R., Andres, J.L., Lara, A., Xu, B., Cao, Z., Cai, Y. (2021). Theoretical model for the shear strength of rock discontinuities with non-associated flow laws. Geomechanics and Engineering, 24(4), 307-321. https://doi.org/10.12989/gae.2021.24.4.307.
7. Zhao, J., Brown, E.T. (1992). Hydro-thermo-mechanical properties of joints in the Carnmenellis granite. Quarterly Journal of Engineering Geology, 25, 279-290. https://doi.org/10.1144/GSL.QJEF/1992.025.04. 03.
8. Esaki, T., Du, S., Mitani, Y., Ikusada, K., Jing, L. (1999). Development of a shear-flow test apparatus and determination of coupled properties for a single rock joint. International Journal of Rock Mechanics and Mining Sciences, 36, 641-650. https://doi.org/10.1016/S0148-9062(99)00044-3.
9. Lee, H.S., Cho, T.F. (2002). Hydraulic characteristics of rough fractures in linear flow under normal and shear load. Rock Mechanics and Rock Engineering, 35(4), 299-318. https://dio.org/10.1007/s00603-002-0028-y.

10. Nemoto, K., Watanabe, N., Hirano, N., Tsuchiya, N. (2000). Direct measurement of contact area and stress dependence of anisotropic flow through rock fracture with heterogeneous aperture distribution. Earth and Planetary Science Letters, 281, 81-87. https://doi.org/10.1016/j.epsl.2009.02.005.
11. Vogler, D., Walsh, S.D.C., Bayer, P., Amann, F. (2017). Comparison of surface properties in natural and artificially generated fractures in a crystalline rock. Rock Mechanics and Rock Engineering, 50, 2891-2909. https://doi.org/10.1007/s00603-107-1281-4.
12. Zhang, X.P., Sun, W., Zhang, Q., Xie, X. (2023). Can the splitting joint reproduce the characteristics of the natural joint in the lab? - A comparison study based on the roughness analysis and shear test. Engineering Geology, 324, 107246. https://doi.org/10.1016/j.enggeo.2023.107246.
13. Peng, H., Zhao, Z., Chen, W., Chen, Y., Fang, J., Li, B. (2020). Thermal effect on permeability in a single granite fracture: Experiment and theoretical model. International Journal of Rock Mechanics and Mining Sciences, 131, 104358. https://doi.org/10.1016/j.ijrmms.2020.104358.
14. Tian, Z., Dai, C., Zhao, Q., Meng, Z., Zhang, B. (2021). Experimental study of joint roughness influence on fractured rock mass seepage. Geofluids, 8813743. https://doi.org/10.1155/2021/8813743.
15. Watanabe, N., Hirano, N., Tsuchiya, N. (2008). Determination of aperture structure and fluid flow in a rock fracture by high-resolution numerical modelling on the basis of a flow-through experiment under confining pressure. Water Resources Research, 44, W06412. https://doi.org/10.1029/2006WR005411.
16. Lee, Y.K., Park, J.W., Song, J.J. (2014). Model for the shear behavior of rock joints under CNL and CNS conditions. International Journal of Rock Mechanics and Mining Sciences, 70, 252-263. https://doi.org/10.1016/j.ijrmms.2014.05.005.
17. Singh, K.K., Singh, D.N., Ranjith, P.G. (2015). Laboratory simulation of flow through single fractured granite. Rock Mechanics and Rock Engineering, 48, 987-1000. https://doi.org/10.1007/s00603-014-0630-9.
18. Belem, T., Homand-Etienne, F., Souly, M. (2000). Quantitative parameters for rock joint surface roughness. Rock Mechanics and Rock Engineering, 33(4), 217-242. https://doi.org/10.1007/s006030070001.
19. Nishiyama, S., Ohnishi, Y., Ito, H., Yano, T. (2014). Mechanical and hydraulic behavior of a rock fracture under shear deformation. Earth, Planets and Space, 66, 108. https://doi.org/10.1186/1880-5981-66-108.
20. Larsson, J., Johansson, F., Ivars, D.M., Johnson, E., Flansbjer, M., Portal, N.W. (2023). A novel method for geometric quality assurance of rock joint replicas in direct shear testing – Part 2: validation and mechanical replicability. Journal of Rock Mechanics and Geotechnical Engineering, 15(9), 2209-2223. https://doi.org/10.1016/j.jrmge.2022.12.012.
21. Ishibashi, T., Fang, Y., Elsworth, D., Watanabe, N., Asanuma, H. (2020). Hydromechanical properties of 3D printed fractures with controlled surface roughness: Insights into shear-permeability coupling process. International Journal of Rock Mechanics and Mining Sciences, 128, 104271. https://doi.org/10.1016/ j.ijrmms.2020.104271.
22. Phillips, T., Bultreys, T., Bisdom, K., Kampman, N., Van Offenwert, S., Mascini, A., Cnudde, V., Busch, A. (2021). A systematic investigation into the control of roughness on the flow properties of 3D-printed fractures. Water Resources Research, 57(4), e2020WR028671. https://doi.org/10.1029/2020WR028671.
23. Tian, W.L., Yang, S.Q., Dong, J.P., Cheng, J.L., Lu, W.L. (2022). An experimental study on triaxial failure mechanical behavior of jointed specimen with different JRC. Geomechanics and Engineering, 28(2), 181-195. https://doi.org/10.12989/gae.2021.28.2.181.
24. Babadagli, T., Develi, K. (2003). Fractal characteristics of rocks fractured under tension. Theoretical and Applied Fracture Mechanics, 39(1), 73-88. https://doi.org/10.1016/S0167-8442(02)00139-8.
25. Cui, Z., Qian, S., Zhang, G., Maochu, Z. (2021). An experimental investigation of the influence of loading rate on rock tensile strength and split fracture surface morphology. Rock Mechanics and Rock Engineering, 54, 1969-1986. https://doi.org/10.1007/s00603-021-02368-4.
26. Shams, G., Rivard, P., Moradian, O. (2023). Observation of fracture process zone and produced fracture surface roughness in granite under Brazilian splitting tests. Theoretical and Applied Fracture

Mechanics, 125, 103680. https://doi.org/10.1016/j.tafmec.2022.103680.
27. Khosravi, A., Simon, R., Rivard, P. (2017). The shape effect on the morphology of the fracture surface induced by the Brazilian test. International Journal of Rock Mechanics and Mining Sciences, 93, 201-209. https://doi.org/10.1016/j.ijrmms.2017.01.007.
28. Zhang, C., Wang, X., Han, P., Zhang, T., Zhang, L., Wang, F. (2024). Acoustic emission and splitting surface roughness of sandstone in Brazilian splitting test under the influence of water saturation. Engineering Geology, 329, 107369. https://doi.org/10.1016/j.enggeo.2023.107369.
29. ISRM (1978). ISRM suggested methods for determining tensile strength of rock materials. International Journal of Rock Mechanics and Mining Sciences & Geomechanics Abstracts, 15(3), 99-103. https://doi.org/10.1016/01489062(78)90003-7.
30. Bieniawski, Z.T., Bernede, M.J. (1979). ISRM suggested methods for determining the uniaxial compressive strength and deformability of rock materials: Part I. International Journal of Rock Mechanics and Mining Sciences & Geomechanics Abstracts, 16(2), 135-140. https://doi.org/10.1016/0148-9062(79)91451-7.
31. Franklin, J. (1979). ISRM suggested methods for determining water content, porosity, density absorption and related properties and swelling and slake-durability index properties. International Journal of Rock Mechanics and Mining Sciences & Geomechanics Abstracts, 16(2), 143-151.
32. ASTM (2016). Standard test method for splitting tensile strength of intact rock core specimen (D3967-16). ASTM international West Conshohocken.
33. Fardin, N., Feng, Q., Stephansson, O. (2004). Application of a new in situ 3D laser scanner to study the scale effect on the rock joint surface roughness. International Journal of Rock Mechanics and Mining Sciences, 41, 329-335. https://doi.org/10.1016/S1365-1609(03)00111-4.
34. Feng, Q., Röshoff, K. (2015). A survey of 3D laser scanning techniques for application to rock mechanics and rock engineering. The ISRM suggested methods for rock characterization, testing and monitoring: 2007-2014, Springer, 265-293. https://doi.org/10.1007/978-3-319-07713-0_25.
35. Ester, M., Kriegel, H.P., Sander, J., Xu, X. (1996). A density based algorithm for discovering clusters in large spatial database with noise. Proceedings of the 2nd International conference on knowledge discovery and data mining (KDD-96), Portland, USA.
36. Zhang, Z. (1994). Iterative point matching for registration of free-form curves and surfaces. International Journal of Computer Vision, 13(2), 119-152. https://doi.org/10.1007/BF01261801.
37. Barton, N., Choubey, V. (1977). The shear strength of rock joints in theory and practice. Rock Mechanics, 10(1), 1-54. https://doi.org/10.1077/BF01261801.
38. Hong, E.S., Lee, J.S., Lee, I.M. (2008). Underestimation of roughness in rough rock joints. International Journal for Numerical and Analytical Methods in Geomechanics, 32, 1385-1403. https://doi.org/10.1002/nag.678.
39. Tse, R., Cruden, D.M. (1979). Estimating joint roughness coefficient. International Journal of Rock Mechanics and Mining Sciences & Geomechanics Abstracts, 16, 303-307. https://doi.org/10.1016/0148-9062(79)90241-9.
40. Yu, X., Vayssade, B. (1991). Joint profile and their roughness parameters. International Journal of Rock Mechanics and Mining Sciences & Geomechanics Abstracts, 28(4), 333-336. https://doi.org/10.1016/0148-9062(91)90598-G.
41. Barton, N., de Quadros, E. (1997). Joint aperture and roughness in the prediction of flow and groutability of rock mass. International Journal of Rock Mechanics and Mining Sciences, 34(3-4), 252. https://doi.org/ 10.1016/S1365-1609(97)00081-6.
42. Myer, N.O. (1962). Characterization of surface roughness. Wear, 5, 182-189. https://doi.org/10.1016/0043-1648(62)90002-9.
43. Mandelbrot, B.B. (1967). How long is the coast of Britain? Statistical self-similarity and fractal dimension. Science, 155, 636-638. https://doi.org/10.1126/science.156.3775.636.
44. Hakami, E., Larsson, E. (1996). Aperture measurements and flow experiments on a single natural fracture. International Journal of Rock Mechanics and Mining Sciences & Geomechanics Abstracts, 33(4), 395-404. https://doi.org/10.1016/0148-9062(95)00070-4.

45. Roko, R.O., Daemen, J.J.K., Myers, D.E. (1997). Variogram characterization of joint surface morphology and asperity deformation during shearing. International Journal of Rock Mechanics and Mining Sciences, 34(1), 71-84. https://doi.org/10.1016/S1365-1609(97)80034-2.
46. Lanaro, F. (2000). A random field model for surface roughness and aperture of rock fractures. International Journal of Rock Mechanics and Mining Sciences, 37, 1195-1210. https://doi.org/10.1016/S1365-1609(00)00052-6.
47. Chen, S.J., Zhu, W.C., Yu, Q.L., Liu, X.G. (2016). Characterization of anisotropy of joint surface roughness and aperture by variogram approach based on digital image processing technique. Rock Mechanics and Rock Engineering, 49, 855-876. https://doi.org/10.1007/s00603-015-0795-x.
48. Zhao, L., Zhang, S., Huang, D., Zuo, S., Li, D. (2018). Quantitative characterization of joint roughness based on semivariogram parameters. International Journal of Rock Mechanics and Mining Sciences, 109, 1-8. https://doi.org/10.1016/j.ijrmms.2018.06.008.
49. Nasab, H., Karimi-Nasab, S., Jalalifar, H. (2021). Geo-statistical algorithm for evaluation of primary and secondary roughness. Geomechanics and Engineering, 24(4), 359-370. https://doi.org/10.12989/gae.2021.24.4.359.
50. Backers, T., Fardin, N., Dresen, G., Stephansson, O. (2003). Effect of loading rate on mode I fracture toughness, roughness and micromechanics of sandstone. International Journal of Rock Mechanics and Mining Sciences, 40, 425-433. https://doi.org/10.1016/S1365-1609(03)00015-7.
51. Bruhwiler, E., Wittmann, F.H. (1990). The wedge splitting test, a new method of performing stable fracture mechanics tests. Engineering Fracture Mechanics, 35(1-3), 117-125. https://doi.org/10.1016/0013-7944(90)90189-N.
52. Li, D., Wong, L.N.Y. (2013). The Brazilian disc test for rock mechanics applications: Review and new insights. Rock Mechanics and Rock Engineering, 46, 269-287. https://doi.org/10.1007/s00603-012-0257-7.
53. Ma, Y., Huang, H. (2018). DEM analysis of failure mechanisms in the intact Brazilian test. International Journal of Rock Mechanics and Mining Sciences, 102, 109-119. https://doi.org/10.1016/j.ijrrms.2017.11. 010.
54. Navidtehrani, Y., Betegon, C., Zimmerman, R.W., Martinez-Paneda, E. (2022). Griffith-based analysis of crack initiation location in a Brazilian test. International Journal of Rock Mechanics and Mining Sciences, 159, 105227. https://doi.org/10.1016/j.ijrmms.2022.105227.
55. Bao, H., Zhang, G., Lan, H., Yan, C., Xu, J., Xu, W. (2020). Geometric heterogeneity of the joint roughness coefficient revealed by 3D laser scanning. Engineering Geology, 265, 105415. https://doi.org/10.1016/ j.enggeo.2019.105415.